Direct and continuous generation of pure acetic acid solutions via electrocatalytic carbon monoxide reduction

Peng Zhu[a,1], Chuan Xia[a,b,1], Chun-Yen Liu[a,1], Kun Jiang[c], Guanhui Gao[d], Xiao Zhang[a], Yang Xia[a], Yongjiu Lei[e], Husam N. Alshareef[e], Thomas P. Senftle[a,2], and Haotian Wang[a,d,f,g,2]

[a]Department of Chemical and Biomolecular Engineering, Rice University, Houston, TX 77005; [b]Smalley-Curl Institute, Rice University, Houston, TX 77005; [c]School of Mechanical Engineering, Shanghai Jiao Tong University, Shanghai 200240, China; [d]Department of Materials Science and Nano-Engineering, Rice University, Houston, TX 77005; [e]Materials Science and Engineering, King Abdullah University of Science and Technology, Thuwal, 23955-6900, Saudi Arabia; [f]Department of Chemistry, Rice University, Houston, TX 77005; and [g]Canadian Institute for Advanced Research (CIFAR) Azrieli Global Scholar, MaRS Centre, Toronto, ON M5G 1M1, Canada

Edited by Alexis T. Bell, University of California, Berkeley, CA, and approved November 20, 2020 (received for review May 28, 2020)

Electrochemical CO_2 or CO reduction to high-value C_{2+} liquid fuels is desirable, but its practical application is challenged by impurities from cogenerated liquid products and solutes in liquid electrolytes, which necessitates cost- and energy-intensive downstream separation processes. By coupling rational designs in a Cu catalyst and porous solid electrolyte (PSE) reactor, here we demonstrate a direct and continuous generation of pure acetic acid solutions via electrochemical CO reduction. With optimized edge-to-surface ratio, the Cu nanocube catalyst presents an unprecedented acetate performance in neutral pH with other liquid products greatly suppressed, delivering a maximal acetate Faradaic efficiency of 43%, partial current of 200 mA·cm^{-2}, ultrahigh relative purity of up to 98 wt%, and excellent stability of over 150 h continuous operation. Density functional theory simulations reveal the role of stepped sites along the cube edge in promoting the acetate pathway. Additionally, a PSE layer, other than a conventional liquid electrolyte, was designed to separate cathode and anode for efficient ion conductions, while not introducing any impurity ions into generated liquid fuels. Pure acetic acid solutions, with concentrations up to 2 wt% (0.33 M), can be continuously produced by employing the acetate-selective Cu catalyst in our PSE reactor.

CO reduction | solid electrolyte | pure acetic acid | CO_2 reduction

Electrochemically reducing carbon dioxide (CO_2) or carbon monoxide (CO) to commodity fuels or chemicals, with the input of green and economical renewable electricity, has become an alternative route to traditional chemical engineering processes (1–7). To date, a variety of catalysts have been demonstrated to reduce CO_2 into C_1 products (CO, formate, etc.) with high Faradaic efficiencies (FEs) (6, 8–14); however, the critical step of C-C coupling toward high-value C_{2+} products was rarely observed on catalysts other than Cu (15–20). Due to its proper binding strength with *CO (19, 21, 22), Cu has shown the capability of catalyzing the coupling of two carbons or more in CO_2/CO reduction reactions (CO_2RR/CORR), which, however, typically suffers from large overpotential and low selectivity (23–25). In previous studies on Cu catalysts, tremendous efforts have been focused on how to promote C-C coupling toward high selectivity of C_{2+} products, including facet engineering (26–28), grain boundary engineering (29, 30), surface modifications (31–33), etc. For example, recent studies on facet dependence of C-C coupling have shown that the C_{2+} selectivity could be improved on Cu(100) compared to other facets due to more stabilized *OCCO intermediates (26, 34). While the overall C_{2+} selectivity is constantly improved by researchers in this field, the generated products are typically a mixture of different C_{2+} compounds, which subsequently necessitates energy- and cost-intensive downstream product separation and purification processes (35–37). A solution to continuously obtain a highly pure, single C_{2+} product stream, which can be directly fed into practical applications, will impose a significant scientific and economic impact but has been rarely studied before.

Ethylene, ethanol, and acetate are the three major C_2 products that have been widely reported in CO_2RR/CORR on Cu materials (16–18, 38–44). Compared to gas-phase products, liquid products show significant advantages due to their high energy densities and ease of storage and distribution (45). Nevertheless, the generation of a high-purity C_2 liquid fuel via electrochemical CO_2RR/CORR is challenging due to the involvement of two types of impurities. First, in previous studies of Cu catalysts, while the C_2 product can be dramatically increased by strategies such as exposing (100) facets, ethanol and acetic acid usually share the same potential window and are cogenerated simultaneously, making it difficult to obtain a single C_2 liquid product (29, 46, 47); Second, in traditional H-cell or flow-cell reactors, the generated liquid products were mixed with solutes in liquid electrolytes such as KOH or $KHCO_3$, which requires extra separation and concentration processes to recover pure liquid fuel solutions in practical applications (37, 48, 49). An integration of rational design in both catalytic material and reactor, for high single-C_2 selectivity and electrolyte-free liquid fuel output, respectively, therefore becomes the key to achieve the goal of pure C_2 liquid fuels.

Significance

Using electricity to reduce CO_2 or CO back into valuable liquid fuels can revolutionize the way we produce chemicals/fuels. However, there are two types of impurity challenges involved: Different liquid products were typically cogenerated on Cu catalysts; in addition, those generated liquid fuels were inevitably mixed with ion impurities in liquid electrolytes. By integrating the rational design of Cu nanocube catalyst and porous solid electrolyte reactor, we report a direct and continuous generation of high-purity acetic acid solutions via electrochemical CO reduction.

Author contributions: T.P.S. and H.W. designed research; P.Z., C.X., and C.-Y.L. performed research; K.J., Y.X., Y.L., H.N.A., T.P.S., and H.W. contributed new reagents/analytic tools; P.Z., C.X., C.-Y.L., G.G., X.Z., T.P.S., and H.W. analyzed data; and P.Z., C.X., C.-Y.L., T.P.S., and H.W. wrote the paper.

The authors declare no competing interest.

This article is a PNAS Direct Submission.

[1]P.Z., C.X., and C.-Y.L. contributed equally to this work.

[2]To whom correspondence may be addressed. Email: tsenftle@rice.edu or htwang@rice.edu.

This article contains supporting information online at https://www.pnas.org/lookup/suppl/doi:10.1073/pnas.2010868118/-/DCSupplemental.

Published December 30, 2020.

Here we report the continuous generation of pure acetic acid solutions via CORR on Cu nanocube (NC) catalysts in a porous solid electrolyte (PSE) reactor. By flexibly tuning the edge to (100) surface ratio, the medium-size Cu NC catalyst exhibits a maximal acetate Faradaic efficiency of 43% with a partial current density of ~200 mA·cm^{-2} in neutral pH, setting up a different acetate performance benchmark (18, 40, 41). More importantly, the selectivity of other liquid products (ethanol and trace amount of n-propanol) was suppressed to below 2%, suggesting an ultrahigh acetic acid relative purity of up to 98 wt%. An impressive stability was demonstrated by a continuous operation of CORR under 150 mA·cm^{-2} current for over 150 h with negligible degradation in selectivity and activity. This acetate-selective Cu NC catalyst was successfully employed into our PSE reactor for the continuous generation of electrolyte-free, pure acetic acid solutions, with overall current of up to 1 A·cm^{-2} and acetic acid relative purity as high as 96 wt%. Different from the traditional liquid electrolyte, our PSE layer can efficiently conduct ions while it does not introduce any impurity ions into the generated liquid products. Density functional theory (DFT) calculations suggest that the stepped edge sites on the Cu NC readily dissociate *OCCOH into *CCO and *OH, which is a key step in promoting the formation of acetate. We propose that the large NC has a low edge-to-facet ratio and therefore cogenerates considerable ethanol and ethylene instead of acetate, while a small NC provides less active (100) area for C-C coupling and therefore predominantly catalyzes the hydrogen evolution reaction (HER) instead of yielding C_2 products.

Results

Synthesis and Characterizations of Cu NC Catalysts. The direct synthesis of metallic Cu NCs involves organic ligands or surfactants that could impact its intrinsic CORR activity (41, 50). Additionally, its surface oxidation when exposed to air or electrolyte before electrochemical tests will also complicate our analysis. We therefore start with the controllable synthesis of ligand-free Cu_2O NCs followed by in situ electrochemical reduction to metallic Cu NCs, with the cubic shape well maintained due to surface epitaxy (26). The Cu_2O NCs were prepared by a chemical reduction method (51), using copper sulfate as the copper source, sodium citrate as the stabilizer, and ascorbic acid as the reducing agent (*Experimental Methods*) to avoid any surfactants or ligands. The catalysts' edge to (100) surface ratio can be easily tuned by changing the size of NCs. In this synthesis method, the size of NCs can be flexibly controlled by tuning the mole fraction of sodium citrate (*Experimental Methods* and *SI Appendix*, Fig. S1 and Table S1). Three typical sizes of NCs, small (50 nm), medium (90 nm), and large (200 nm), were prepared to study the size effects on CORR. Scanning electron microscopy (SEM) images confirmed the different sizes of Cu_2O NCs with uniform size distributions (Fig. 1*A* and *SI Appendix*, Fig. S2). Aberration-corrected transmission electron microscopy (TEM) of the medium-size Cu_2O NC showed a clear (100) lattice with a measured spacing of 0.21 nm (Fig. 1*B*), which matches well with the intrinsic (200) facet spacing, as well as the X-ray diffraction result (*SI Appendix*, Fig. S3). Distinct patterns of selective area electron diffraction (SAED) suggest the single-crystalline nature of those as-synthesized Cu_2O NCs, with (100) facets exposed only (Fig. 1*C*). Focused on local atomic sites, Fig. 1*D* and *SI Appendix*, Fig. S4 provide direct evidence of stepped sites along the edge and corner of Cu_2O NCs. Those as-prepared small, medium, and large Cu_2O NCs were first spray coated onto gas diffusion layer (GDL) electrodes, with obviously different colors due to their variations in sizes (*SI Appendix*, Fig. S2*E*), followed by a prereduction process and then a CORR test (*Experimental Methods*). The electrochemical prereduction process, during which Cu_2O NCs were converted into metallic Cu phase under a negative potential (*Experimental Methods*), was confirmed by synchrotron-based in operando X-ray absorption spectroscopy (*SI Appendix*, Fig. S5). While the existence and distribution of oxygen contents in Cu_2O NCs can be easily detected and mapped out by ex situ energy dispersive spectroscopy (EDS) in scanning transmission electron microscope (STEM) (Fig. 1*E* and *SI Appendix*, Fig. S6), this characterization may not be used for freshly reduced Cu as its surface is very sensitive to air and water and could easily get oxidized right after the release of negative potential. Therefore, to further elucidate whether there will be any surface oxygen remaining under reduction conditions, we carefully monitored the prereduction process by in situ Raman spectroscopy (Fig. 1 *F* and *G*) (52, 53). Pristine Cu_2O NCs under open-circuit potential showed the typical Raman peaks at 152, 219, 412, 542, and 630 cm^{-1}, respectively, with a dominant peak at 219 cm^{-1} as the indicator of the existence of oxides (26, 54). Once a negative potential of –0.34 V vs. reversible hydrogen electrode (RHE) was applied, the intensity of the peak gradually decreased and eventually disappeared within ~90 s. After 10 min reduction, no Cu_2O oxide peaks were detected, suggesting the complete reduction of surface oxides into the metallic phase (55–57).

While the cubic morphology and size were well maintained after the prereduction process (Fig. 1*H* and *SI Appendix*, Fig. S7), which is in good agreement with previous observations (26, 58, 59), the NCs became polycrystalline with a few grains observed (Fig. 1*I*). Although those grains may have different orientations, a significant portion of the cube surface was still covered by Cu(100) facets as shown by the cubic lattices in the high-resolution TEM image in Fig. 1*I* (26). This was further confirmed by the SAED diffraction pattern in Fig. 1*J* where we observed a few brightest dots diffracted from (200) lattices. Importantly, similar to Cu_2O NCs, stepped sites were also observed along the edge of Cu NCs in Fig. 1*K* (*SI Appendix*, Figs. S8 and S9).

CORR Electrochemical Characterizations. The CORR performances of small, medium, and large Cu NCs were first evaluated in a standard three-electrode flow-cell reactor using 0.5 M $KHCO_3$ aqueous electrolyte (pH = 8.6; *Experimental Methods*). Gas and liquid products were separately analyzed using gas chromatography (GC) and NMR, respectively (*Experimental Methods*). In traditional flow-cell tests, there are two challenges that typically limit the catalyst's lifespan within only a few hours. One is the GDL flooding, particularly under large current densities; the other is the direct contact between Cu catalysts and liquid electrolyte which promotes the Cu atom mobility for morphology evolution. To solve these challenges, here we applied a layer of anion exchange membrane (AEM) to separate the catalyst layer and liquid electrolyte in our flow-cell tests (*SI Appendix*, Fig. S10). Electrochemically generated acetate or ethoxide anions can be efficiently conducted through AEM and collected by the flowing electrolyte, while the catalytic materials were successfully separated from the direct contact with water. To avoid any concerns that the additional layer of AEM could block some liquid products to be collected from the middle-layer flowing electrolyte, we also collected and quantified liquid products from the CO gas stream. As shown in *SI Appendix*, Table S2, the majority of generated products were collected from the middle-layer flowing electrolyte, with negligible FEs of acetic acid (0.1%), ethanol (1.2%), and n-propanol (1%) collected from the CO effluent stream. In this designed flow-cell reactor, the obtained Cu catalyst's performances will be more straightforwardly translated to our solid electrolyte devices where pure liquid fuel solutions can be obtained (48, 49).

The three different-size Cu NC catalysts showed similar activities under the same applied potentials with the same catalyst mass loading (0.5 mg·cm^{-2}; Fig. 2*A*). As expected and also in agreement with previous reports (27, 60), small-size Cu NCs (~50 nm) showed significant HER with selectivity ~60%, which

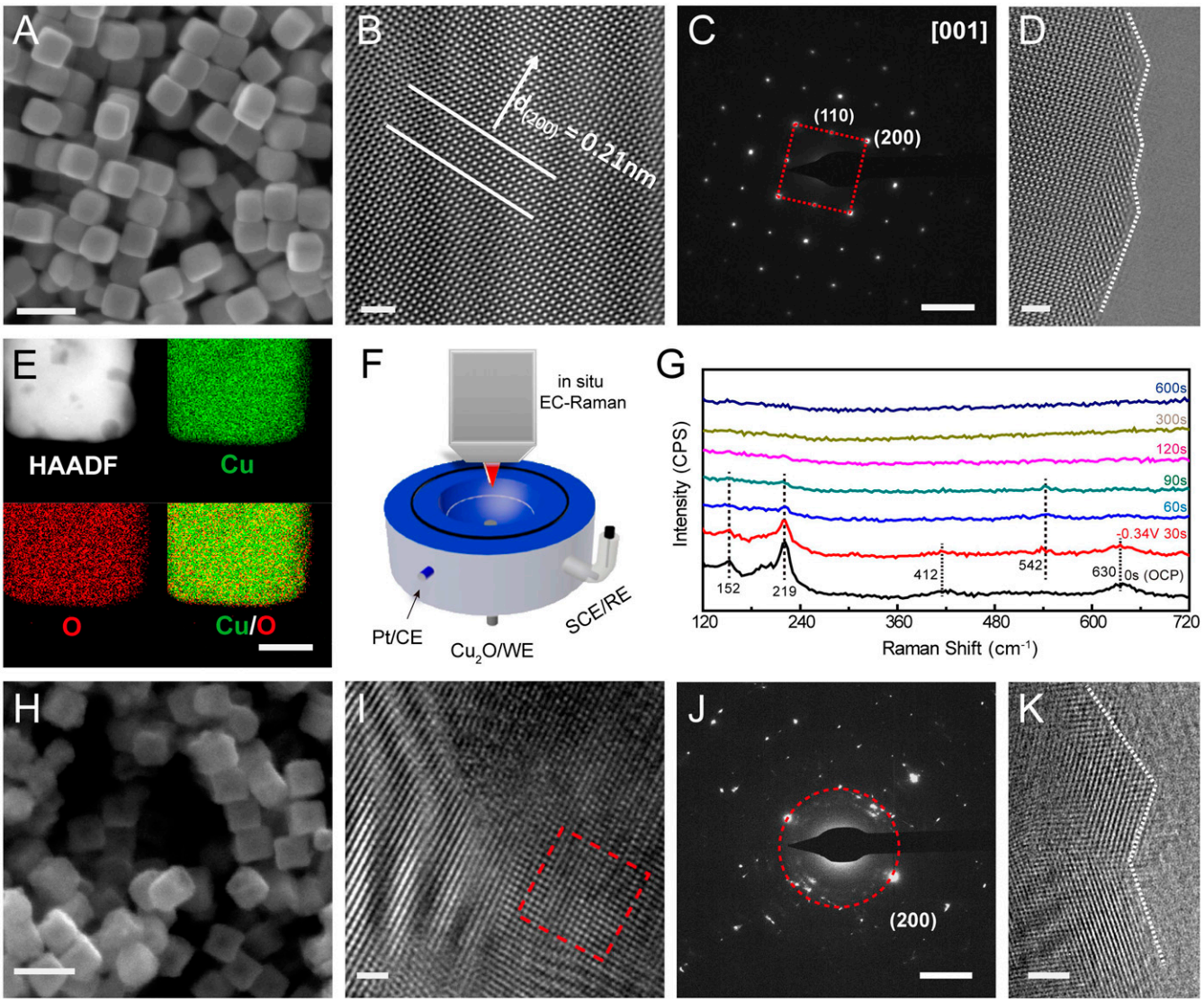

Fig. 1. Characterizations of medium-size Cu_2O and Cu NCs. (*A* and *B*) SEM (*A*) and high-resolution TEM (*B*) images of Cu_2O NCs. The (100) interplanar distance was measured to be 0.21 nm. (*C*) The corresponding SAED pattern along the [001] zone axis. (*D*) Step sites along the edge of Cu_2O NCs. (*E*) High-angle annular dark-field scanning transmission electron microscopy (HAADF-STEM) image and EDS mapping of a Cu_2O NC. Cu and O signals are uniformly distributed. (*F*) Schematic of the in situ electrochemical Raman apparatus. (*G*) The in situ observation of the Raman spectra during the prereduction process under –0.34 V vs. RHE. (*H* and *I*) SEM (*H*) and TEM (*I*) images of Cu NCs reduced from Cu_2O NCs. Cu (100) lattice fringes are marked by the red line in *I*. (*J*) The SAED pattern of one Cu NC, with the brightest diffraction dots corresponding to the Cu (200) facets. (*K*) Step sites along the edge of Cu NCs. (Scale bars: *A*, 200 nm; *B*, 1 nm; *C*, 5 nm^{-1}; *D*, 2 nm; *E*, 30 nm; *H*, 200 nm; *I*, 1 nm; *J*, 5 nm^{-1}; *K*, 2 nm.)

is possibly due to the high ratio of edge and corner sites where hydrogen evolution can easily take off (Fig. 2*B*). With the NC catalyst increased to the medium size of ~90 nm, HER FE was suppressed to below 30% under large current densities, while the overall C_{2+} selectivity was improved to above 65%. As our target is to obtain high-purity single-liquid product, we carefully analyzed the liquid product distribution. Although all three types of liquid products, acetate, ethanol and n-propanol, can be detected by NMR across the whole electrochemical window, the dominant liquid product is acetate (Fig. 2*C* and *SI Appendix*, Fig. S11). As only a trace amount of n-propanol was produced (less than 0.5%), the major competition or contamination was therefore from ethanol. As shown in Fig. 2*C*, with more and more negative potential applied, the selectivity of acetate gradually increased while ethanol decreased, resulting in a continuously increased acetate relative purity (Fig. 2*E*) (the concept of product relative purity is defined in *Experimental Methods*). The peak relative selectivity of acetate reached to above 43 wt% under 450 $mA{\cdot}cm^{-2}$ current, delivering an unprecedented acetate partial current of ~200 $mA{\cdot}cm^{-2}$ in neutral pH (*SI Appendix*, Fig. S12 and Table S3), where the ethanol selectivity was suppressed to below 2 wt %. This high contrast of product selectivity gives a peak acetate relative purity of above 98 wt%, suggesting a nearly exclusive generation of acetate as the single C_2 liquid product. With negligible effect of the binders (*SI Appendix*, Fig. S13), the liquid product distribution underwent an obvious change once the size of Cu NC was increased to ~200 nm (Fig. 2*D* and *SI Appendix*, Fig. S14). While the acetate selectivity was slightly decreased compared to the medium-size NC, the competing ethanol FE was nearly doubled, resulting in a dramatically decreased product purity (*SI Appendix*, Figs. S9 and S12). To compare the reaction rates further, the performances (*SI Appendix*, Figs. S15

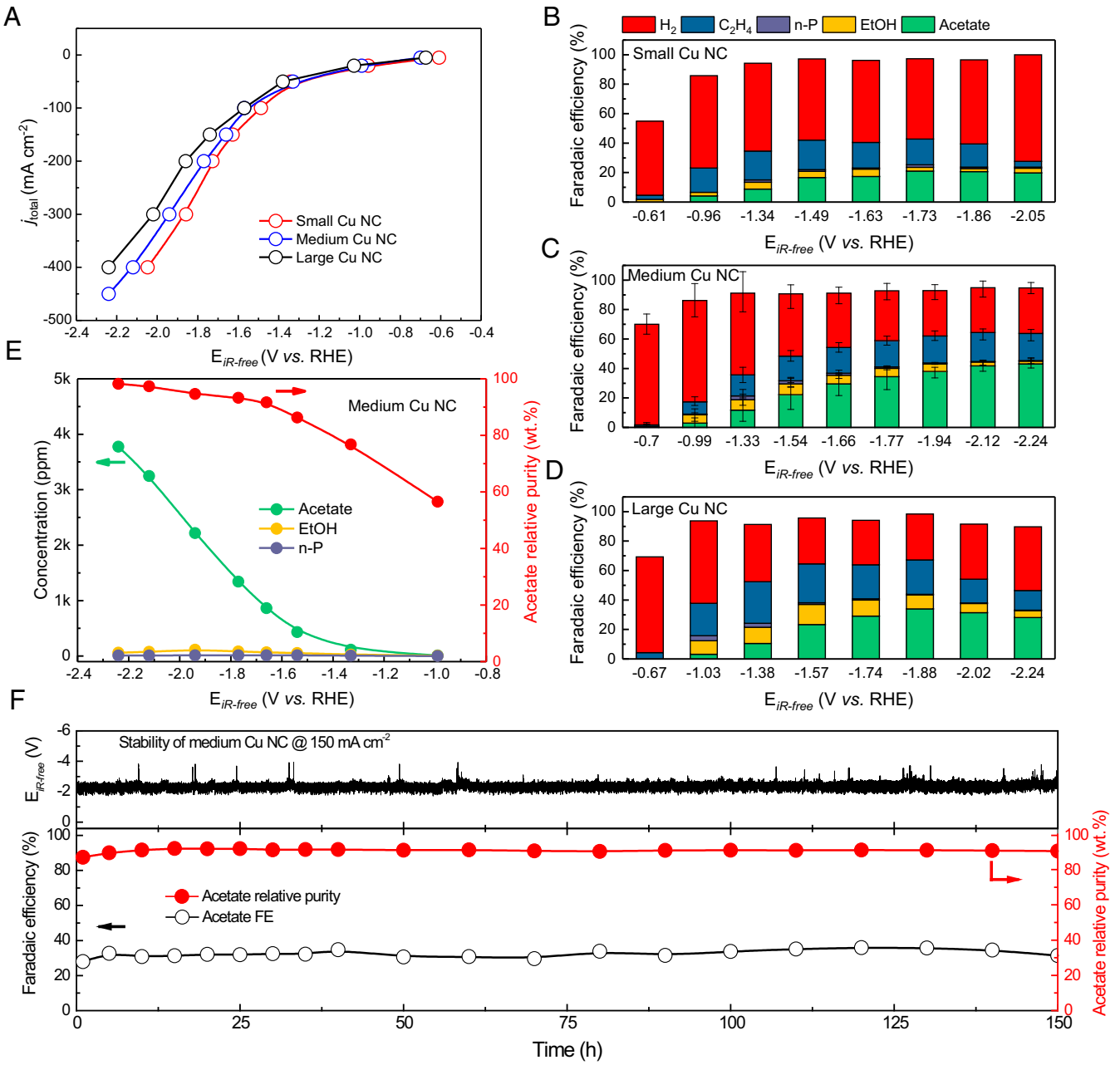

Fig. 2. Electrocatalytic CO reduction to acetate using the Cu catalyst in the flow cell. (*A*) The overall current density of small, medium, and large Cu NCs. The reported potentials were not current-resistance (*iR*) compensated. The measured working electrode resistance in this flow-cell reactor after catalysis was ~5 ohms using electrochemical impedance spectroscopy (EIS) measurements. (*B–D*) FEs of each CO reduction product on small (*B*), medium (*C*), and large (*D*) Cu NCs under different potentials. The error bars in *B* represent three independent medium-size Cu NC samples. The FEs of small and large Cu NCs shown were averaged from two independent samples. (*E*) The concentrations of liquid products and relative acetate purities of medium Cu NCs under different potentials, where 27 mL·h^{-1} DI water flow was used. (*F*) Chronopotentiometry stability test under 150 mA·cm^{-2} current density in the flow cell for 150 h. The potential, acetate FE, and acetate relative purity were well maintained during the course, suggesting the high stability of Cu NC catalyst. The total geometric area of the flow field in the cathode is 1 cm^2.

and S16) were normalized to the electrochemical surface area (ECSA) (*SI Appendix*, Fig. S15 gives the measurements).

The trends of CORR product distribution with the size of Cu NC catalysts suggest that a balance between edge and (100) surface sites is needed to tune the reaction pathways for high-purity acetate generation. As the medium-size Cu NC catalyst showed impressive selectivity and activity toward high-purity acetate, its stability to maintain this high performance is of great importance for practical applications. Postcatalysis SEM characterization revealed that the Cu NC structure is well maintained (*SI Appendix*, Fig. S17). A 150-h CORR electrolysis was continuously and stably operated under 150 mA·cm^{-2} current, maintaining an acetate relative purity of above 90 wt% with negligible degradations in selectivity and activity (Fig. 2*F*).

Production of Pure C_2 Liquid Fuel Solutions. The excellent acetate generation performance, high stability, and high acetate relative purity together make the medium-size Cu NC an ideal catalyst

for the purpose of continuous and direct generation of pure acetic acid solutions (48, 49). However, the challenge of liquid product mixture with liquid electrolyte still needs to be resolved (37). In traditional H-cell or flow-cell reactors, liquid electrolytes, such as $KHCO_3$ or KOH solutions, were typically used for both ion conduction and liquid product collection (61, 62). Although single C_2 liquid product can now be selectively generated with minimized impurities from other competing products, those generated liquid fuels are actually in a mixture with solutes in liquid electrolytes, making its practical application challenging due to energy- and cost-intensive downstream separation processes (24, 37). To address this challenge, here we designed a PSE layer, which can efficiently transport ions between the cathode and anode as liquid electrolyte does, but does not introduce any soluble ions to mix with generated acetic acid (48, 49). As shown in the schematic in Fig. 3*A* and *SI Appendix*, Fig. S18, the cathode and anode of our PSE device are catalyst-coated GDL electrodes, which sandwiched AEMs and cation exchange membranes (CEMs), respectively. The cathode electrode was continuously supplied with a CO stream for CORR to acetate, while the anode side was circulated with 0.5-M H_2SO_4 solution for water oxidation. In the middle chamber, a PSE layer was placed in between the AEM and CEM to facilitate ion transportations with minimized ohmic losses (*SI Appendix*, Fig. S19) and also allow for a deionized (DI) water stream to collect pure liquid fuels generated. Specifically, electrochemically generated acetate ions from CORR on Cu NC catalyst were driven by the electrical field across the AEM toward the middle PSE layer. Meanwhile, protons generated by water oxidation on IrO_2 catalyst on the anode move across the CEM into the middle chamber to compensate the charge (48, 63). The acetic acid molecules formed in the PSE layer via the ionic recombination were then efficiently brought out via the DI water stream through this porous layer. Obviously, a wide range of concentrations of pure acetic acid solutions can be obtained by tuning the acetate production rate or DI water flowrate.

The current-voltage (I-V) curve of CORR in our 4-cm^2 Cu-NC//PSE//IrO_2 device is plotted in Fig. 3*B* with a fixed DI water flowrate of 108 $mL{\cdot}h^{-1}$. This flowrate was chosen to be fast enough to avoid significant product accumulations within the PSE layer, which otherwise could bring negative impacts on the evaluation of the catalyst's intrinsic activity. By ramping up the cell voltage, the overall current density of the PSE reactor gradually increased together with the acetic acid selectivity (Fig. 3*C*). A maximal acetic acid FE of 30% was achieved under an overall current of 700 $mA{\cdot}cm^{-2}$ (2.8 A; Fig. 3*C*), delivering a partial current of 210 $mA{\cdot}cm^{-2}$ (840 mA) in generating pure acetic acid solutions (Fig. 3*D*). The partial current was further increased to a peak of 250 $mA{\cdot}cm^{-2}$ (1 A; Fig. 3*D*), corresponding to a continuous generation of 86 mM acetic acid solution under this DI water flowrate. The pH of this acetic acid product was measured to be ~3.0 and is in good agreement with its theoretical value of 2.9 (acid dissociation constant $K_a = 1.8{\times}10^{-5}$), indicating a high-purity output. While we observed that the acetic acid selectivity in the solid electrolyte reactor was lower compared to our flow-cell performance, which is due to the different pH (acidic and neutral pH in PSE and flow-cell reactors, respectively), the liquid product distribution, which is key to the generated liquid fuel purity, still follows a similar trend. As shown in Fig. 3*E*, the acetic acid relative purity surpasses 90 wt% under cell currents of over 200 $mA{\cdot}cm^{-2}$ and reaches a maximum of 96 wt% under 1 $A{\cdot}cm^{-2}$ (4 A) current. Additionally, possible impurity ions including sodium, potassium, iron, and copper were detected by inductively coupled plasma atomic emission spectroscopy (ICP-OES) and were all below 10 ppm (*SI Appendix*, Table. S4), further demonstrating the ultra-high purity of acetic acid solutions produced by coupling our selective catalyst and solid electrolyte reactor. A higher concentration of pure acetic acid solutions can be easily produced by slowing down the DI water flow while maintaining the operation current. As a result, an unprecedented concentration of ~2 wt% (0.33 M) acetic acid solution was achieved under a DI water flowrate of 5.4 $mL{\cdot}h^{-1}$ (*SI Appendix*, Fig. S20). We noticed that the acetic acid FE gradually decreased with the increase of product concentration, which is possibly due to the decreased pH in the middle chamber, increased reverse reaction of the CO-to-CH_3COOH equilibrium, and increased product crossover to the anode side (48, 49). The stability of our PSE reactor was evaluated by holding a 700-$mA{\cdot}cm^{-2}$ (2.8 A) high cell current. As shown in Fig. 3*F*, a continuous generation of ~50 mM pure acetic acid solution can be stably operated for over 10 h with small fluctuations in product selectivity. More importantly, the relative purity of acetic acid was maintained over 95 wt% during the course of the stability test, suggesting the good stability in liquid product distribution. As a different operation condition for different applications, our solid electrolyte cell can serve as a room temperature, ambient pressure CO hydrogenation reactor for the production of pure acetic acid ($CO+H_2{\rightarrow}CH_3COOH$). In this situation, H_2 will be instead fed into the anode for hydrogen oxidation reaction (HOR) on a commercial Pt-C catalyst to release protons (*SI Appendix*, Fig. S21). The I-V curve and corresponding FEs of our 4-cm^2 Cu-NC//PSE//Pt-C cell are plotted in *SI Appendix*, Fig. S21, presenting similar C_2 product distributions and a significant decrease in cell voltage due to the inherent energy input from H_2.

Investigation on the Impact of Cu Morphology to C_2 Product Selectivity. We applied DFT to examine whether the edge-to-(100) facet ratio on Cu NC catalysts will alter the product distribution in CORR. Since the major products from experiments are C_{2+} chemicals, we begin our analysis with the adsorbed *OCCOH intermediate implicated in many C-C coupling mechanisms (34, 64, 65). *HOCCOH and *CCO are two predominant daughter intermediates derived from *OCCOH (66), where *HOCCOH could be generated through a proton-coupled electron transfer (PCET) (67, 68) and *CCO could be generated through C-OH bond dissociation (34). Here, we take the formation of *HOCCOH versus *CCO to be the key branching point in determining selectivity toward ethylene/ethanol versus acetic acid. This is motivated by several mechanisms proposed previously in the literature. Goddard and coworkers (68), using ab initio molecular dynamics and isotope experiments with $H_2{}^{18}O$, proposed that ethanol and ethylene are derived from the *HOCCOH intermediate. In contrast, both Calle-Vallejo and Koper (34) and Luo et al. (69) showed with DFT that *CCO is a precursor for ethanol and ethylene formation at low overpotential (−0.4 V_{RHE}). Although ethylene and ethanol can be formed from either *CCO or *HOCCOH, we consider here the hypothesis that *CCO is essential for acetate formation. This is motivated by Kanan and coworkers' (29) suggestion that acetate is formed through the reaction of OH^- with a surface-bound ketene (e.g., *CCO, *HCCO, or $*H_2CCO$). Similarly, Luc et al. (41) also proposed that acetate forms through *CCO, but instead through successive PCET steps generating *CHCO and desorbed CH_2CO that then reacts with a water molecule in solution to form acetate. Thus, we propose that sites favoring the formation of *CCO over *HOCCOH will exhibit higher selectivity toward acetic acid because *CCO can produce acetate (Fig. 4*A*). Here, we investigate the formation of *CCO versus *HOCCOH on flat Cu(100) and stepped surfaces, such as Cu(211), Cu(611), and a pocket-shape geometry, to determine whether the site structure influences the tendency to form each intermediate.

The impact of step edges on Cu surfaces on CO_2/CO reduction has been investigated with various representative facets, such as (211) (26) and other high-index surfaces (70–72). However, these previous works focused heavily on *OCCO generation, i.e., C-C bond formation, and the structure sensitivity of the *OCCOH → *CCO + *OH step has not been investigated.

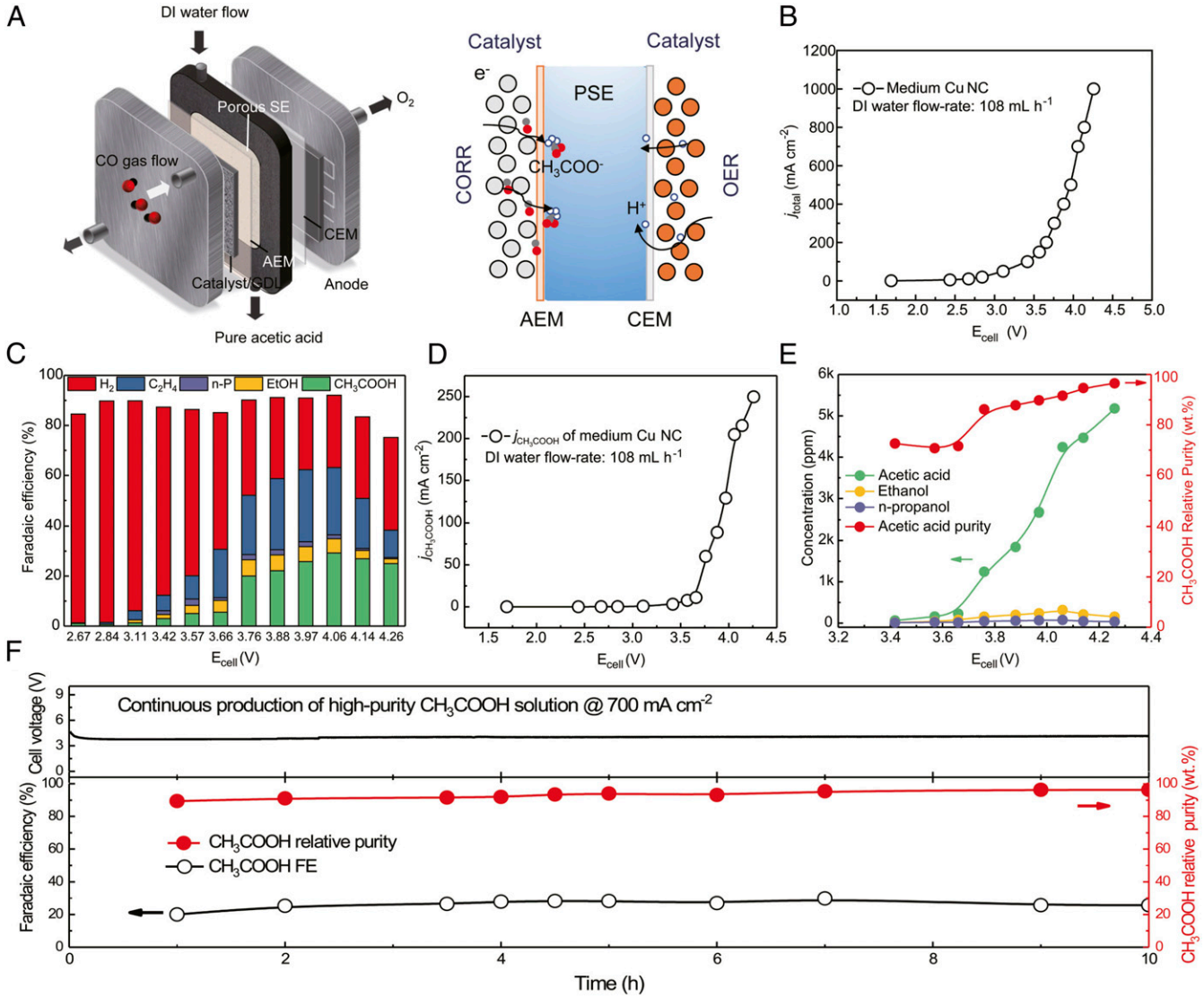

Fig. 3. Production of pure acetic acid solutions using medium Cu catalyst with solid electrolyte reactor system. (*A*) Schematic illustration of CO reduction to pure acetic acid in our solid electrolyte cell. The pure acetic acid product can be formed via the ionic recombination of crossed ions in the middle layer and carried out through the DI water flow. (*B*) The I-V curve of medium-size Cu NCs in a solid electrolyte cell. The cell voltages were *iR* compensated. (*C*) The corresponding FEs of CORR products under different cell voltages. The reported FEs were averaged by three independent samples. (*D*) The partial current density of acetic acid. (*E*) The concentrations and relative purities of generated liquid products under a DI water flowrate of 108 mL·h^{-1} in our solid electrolyte cell. (*F*) Chronopotentiometry stability test by holding 700 mA·cm^{-2} current density for 10 h. The cell voltage, acetate FE, and acetate relative purity were well maintained, suggesting a continuous and stable generation of pure acetic acid solutions. The total geometric area of the flow field in the cathode of our solid electrolyte cell is 4 cm^2.

Here, we use the Cu(100) surface to represent the flat cube facet and Cu(211), Cu(611) (73), and pocket-shape surfaces to represent the high-index cube edges (*SI Appendix*, Figs. S22 and S23). Fig. 4*B* shows that the reaction energy and barrier to form *HOCCOH through PCET are similar on both surfaces (e.g., 0.12-eV difference at −1 V_{RHE}). We conclude that this step is not sensitive to the surface structure, which is intuitive because *HOCCOH forms through a PCET step that does not require interaction with the surface in the transition state. As expected, we find that the formation rate of *HOCCOH is predominantly determined by the applied voltage and pH because the stability of *HOCCOH is similar on both surfaces. The Cu(611) surface, however, has a 0.38 eV lower barrier for *OCCOH to dissociate into *CCO and *OH due to the assistance of the step defect, as illustrated in Fig. 4*C*. Cu(211) and pocket-shape surfaces were further investigated to confirm that high-index surfaces occurring on cluster edges generally reduce the C-O dissociation barrier regardless of the exact defect geometry. As seen in Fig. 4*C*, the C-O bond dissociation barrier is reduced on all of the high-index surfaces, whereas in Fig. 4*B* we see that the PCET barrier for O-H bond formation is not sensitive to the surface structure. These results are consistent with the hypothesis, already suggested in the literature (29), that ketene is a key intermediate along the route to acetate. However, they do not rule out all other proposed mechanisms for acetate formation (74–76) and we are currently pursuing further calculations to explore how high-index surfaces will influence these alternative mechanisms. Therefore, the reactivity of this dissociation step is significantly influenced by the surface geometry and is enhanced by the undercoordinated Cu atoms at the step edge, which implies that controlling the surface morphology (i.e., edge-to-(100) ratio or the size of cube) is a viable strategy for increasing selectivity toward acetate.

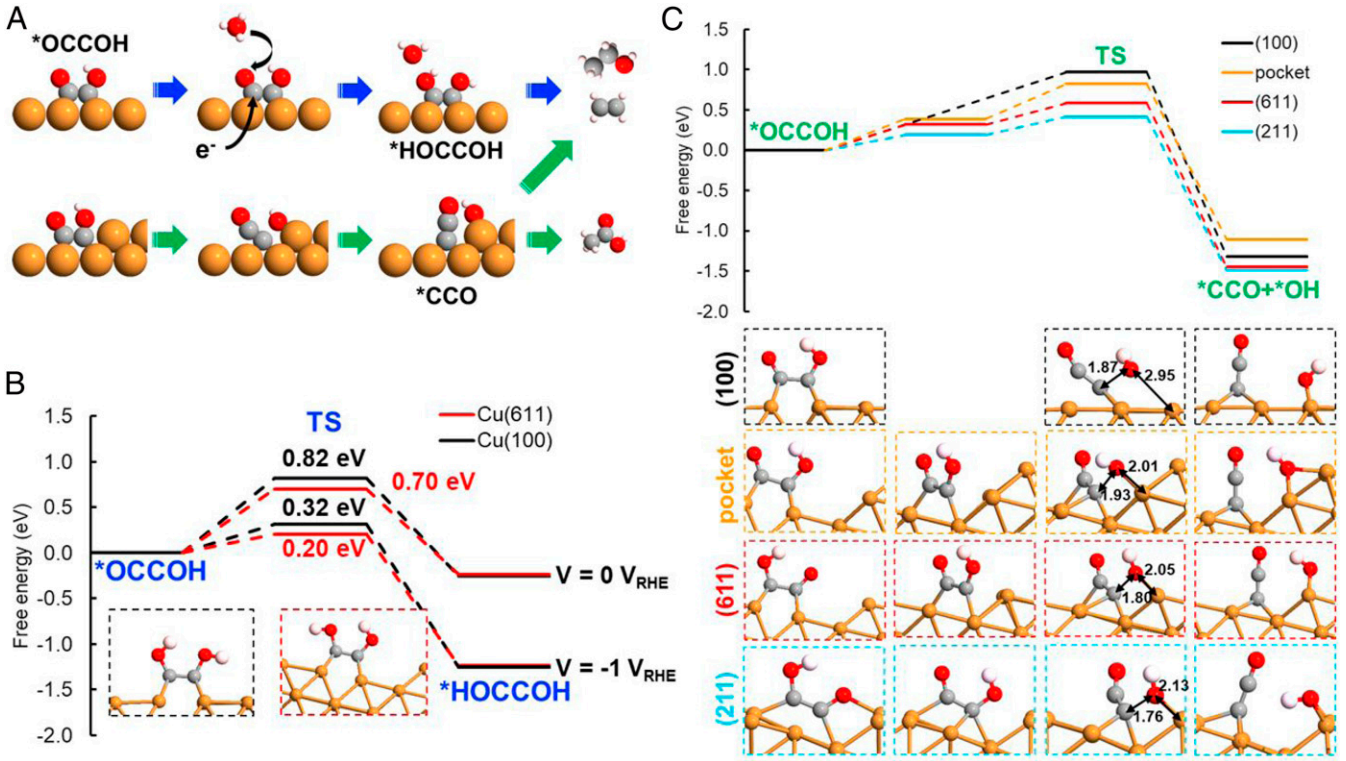

Fig. 4. Proposed reaction mechanism and the reaction energies on different Cu surfaces. (*A*) Proposed reaction mechanism for electroreduction of CO to C_{2+} products. The blue path produces ethanol and ethylene, while the green path can also generate acetic acid. (*B* and *C*) Reaction free energies and barriers (*B*) to form *HOCCOH through PCET at 0 V_{RHE} and −1 V_{RHE} and (*C*) to dissociate *OCCOH to *CCO and *OH on Cu(100) in black, Cu pocket-shape in orange, Cu(611) in red, and Cu(211) in blue. *Insets* show the system geometries. Orange, red, gray, and white spheres represent Cu, O, C, and H, respectively. Numbers in *Insets* represent distance in angstroms. The left figure in the boxes in *C* represents the most stable *OCCOH geometry, while to the immediate right the adsorbate is oriented toward the edge prior to OCC-OH bond dissociation (e.g., the overall barrier is always referenced to the adsorbate on the flat terrace in its most stable configuration).

Our DFT results agree well with the experimental observations, where medium-sized Cu NC catalyst, with an optimized edge-to-(100) ratio, presents the best acetic acid selectivity compared to smaller or larger Cu NCs: Small Cu NCs expose fewer (100) facets with limited C-C coupling toward C_{2+} products (27, 77); large Cu NCs expose more (100) facets where ethanol is cogenerated to lower the acetic acid relative purity.

Conclusion

We successfully demonstrated the continuous generation of pure C_2 liquid fuel solutions via electrochemical CO reduction. By engineering the edge-to-surface ratio of Cu NC catalyst, the C_2 liquid product distribution was successfully controlled with a preferential generation of acetic acid over alcohols. Our DFT simulation results reveal that the coupling of (100) facets and stepped sites along the edge is critical to optimize both the FE and relative purity of acetic acid. Our porous solid electrolyte layer design replaced the use of traditional liquid electrolyte between cathode and anode, enabling an efficient ionic conduction while not introducing any impurity ions into the liquid product stream.

Experimental Methods

Materials. All chemicals including copper sulfate, trisodium citrate, sodium hydroxide, ascorbic acid, potassium hydroxide, ethanol, Nafion 117 solution, deuterium oxide, and dimethyl sulfoxide were purchased from Sigma Aldrich. Millipore water (18.2 MΩ·cm) was used throughout all experiments.

Preparation of Cubic Cu_2O Nanocrystals. A 1.2-mol/L Cu^{2+} stock solution was first prepared by dissolving a certain amount of $CuSO_4$ into Millipore water. In a typical synthesis, 100 mL Millipore water containing 66 mg trisodium citrate was poured into a round-bottom flask with 600-rpm stirring at 20 °C. Then 0.25 mL of 1.2 M $CuSO_4$ solution was quickly injected, followed by adding 0.25 mL of 4.8 M NaOH after 5 min stirring, and the clear solution was turned into turbid blue thereafter. After another 5 min, 0.25 mL of 1.2 M ascorbic acid was injected, and the final suspension was continuously stirred for 30 min and in orange color. The as-prepared Cu_2O NC product was collected by centrifugation at 8,000 rpm for 10 min, washed three times with Millipore water, and then vacuum dried for further use.

Preparation of the Electrodes. Typically, 10 mg of as-prepared Cu_2O NC was mixed with 1 mL of 2-proponal (Sigma Aldrich) and 40 μL of binder solution (alkaline ionomer [Dioxide Materials, 5%] for the proposed cell) and sonicated for 20 min to obtain a homogeneous ink. Then, the prepared ink was air brushed onto 2 × 2-cm^2 Sigracet 39 BC gas diffusion layer (Fuel Cell Store) electrodes.

Materials Characterization. The SEM was performed on an FEI Quanta 400 field emission scanning electron microscope. ICP-OES was done by a third-party company (A & B Lab). TEM and EDS characterizations were carried out using an FEI Titan Themis aberration-corrected transmission electron microscope at 300 kV. Powder X-ray diffraction data were collected using a Bruker D2 Phaser diffractometer in parallel beam geometry employing Cu Kα radiation and a one-dimensional LYNXEYE detector, at a scan speed of 0.02° per step and a holding time of 1 s per step.

X-ray absorption spectra (XAS) on the Cu K edge were acquired at the Brookhaven National Laboratory (BNL), using an Si(111) double crystal monochromator, and performed in fluorescence mode using a four-element Si(Li) drift detector in a vacuum chamber. For in situ tests, continuous CO_2 flow was delivered into a homemade Teflon H cell filled with CO_2-saturated 0.5 M $KHCO_3$; a Kapton-film–covered carbon fiber paper (Cu_2O) working electrode served as the X-ray window for synchrotron radiation. Multistep

potential control was used for the in situ measurements, with a hold time of ~30 min at each potential for the spectrum acquisition. Analyses of the near-edge (on an energy scale) XAS were performed using Athena software.

Electrocatalytic Measurement. The reduced metallic Cu catalyst was prepared at 25 °C in a customized gas-tight H-type glass cell using the as-prepared Cu_2O catalysts. The cathode side was supplied with 30 sccm CO_2 gas. Under −1.5 V vs. RHE applied potential (~50 mA^{-2} current density), the reduction process lasted for 1 h and a clear catalysts color change could be observed. The electrochemical measurements were run with a BioLogic VMP3 workstation. For electrochemical flow-cell tests, typically 0.5 mg/cm^2 Cu_2O and 0.2 mg/cm^2 IrO_2 were air brushed onto two 1 × 2.5-cm^2 Sigracet 39 BC GDL (Fuel Cell Store) electrodes as CORR cathode and oxygen evolution reaction anode, respectively. The two electrodes were placed on opposite sides of two 0.5-cm-thick polytetrafluoroethylene (PTFE) sheets with 0.5-cm-wide by 2.0-cm-long channels such that the catalyst layer interfaced with the flowing liquid electrolyte (*SI Appendix*, Fig. S10), A polystyrene vinylbenzyl methyl imidazolium chloride (PSMIM) AEM (Dioxide Materials) and a Nafion film (Fuel Cell Store) were used for anion and cation exchange, respectively. The geometric surface area of catalyst is 1 cm^2. On the cathode side a titanium gas-flow chamber supplied 30 sccm CO (Airgas; 99.995%) while the anode was open to the atmosphere. The flow rate of the 0.5-M $KHCO_3$ electrolyte was controlled by a syringe pump and set at 0.5 sccm at small-current regions to concentrate liquid reduction products and at 3 sccm at large-current regions to get rid of O_2 bubbles for the anode channel. A saturated calomel electrode (SCE) (CH Instruments) was connected to the cathode channel as the reference electrode and calibrated with an alkaline mercurous oxide electrode before each measurement. All potentials measured against the SCE were converted to the RHE scale in this work using E (vs. RHE) = E (vs. SCE) + 0.244 V + 0.0591*pH, where pH values of electrolytes were determined by an Orion 320 PerpHecT LogR Meter (Thermo Scientific). Solution resistance (R_u) was determined by potentiostatic electrochemical impedance spectroscopy (PEIS) at frequencies ranging from 0.1 Hz to 200 kHz and manually compensated as E (iR corrected vs. RHE) = E (vs. RHE) − R_u * I (amps of average current) (*SI Appendix*, Fig. S24). For the cell with solid electrolyte, a PSMIM AEM (78, 79) (Dioxide Materials) and a Nafion film (Fuel Cell Store) were used for anion and cation exchange, respectively. A Sigracet 39 BC GDL electrode loaded with 0.5 mg·cm^{-2} Cu_2O (4-cm^2 electrode area) and an IrO_2/C electrode (Fuel Cell Store) were used as cathode and anode, respectively. The cathode was supplied with 50 sccm of humidified CO gas, and the anode was circulated with 0.5 M H_2SO_4 aqueous solution at 2 mL·min^{-1}. The porous solid Dowex 1 × 4 copolymer was employed as the CH_3COO^- conductor (Sigma). The Cu_2O //SSE//IrO_2-C cell was first stabilized for 120 min before liquid product collection.

CORR Products Analysis. During electrolysis, continuous CO flow with gas reduction product was vented into a Shimadzu GC-2014 GC. H_2 concentration was quantified by a thermal conductivity detector, and other alkane species contents were analyzed by a flame ionization detector with a methanizer. The partial current density for a given gas product was calculated as

$$j_i = x_i \times v \times \frac{n_i F p_0}{RT} \times (electrode\ area)^{-1},$$

where x_i is the volume fraction of a certain product determined by online GC referenced to calibration curves from two standard gas samples (Scott and Airgas), v is the flow rate, n_i is the number of electrons involved, p_0 = 101.3kPa, F is the Faradaic constant, and R is the gas constant. The corresponding FE at each potential is calculated by $FE = j_i / i_{total} \times 100\%$.

The relative purity for a given liquid product was calculated as

$$wt_i = \frac{j_i}{n_i F u} * M$$

$$relative\ purity = \frac{wt_{acetate}}{wt_{acetate} + wt_{EtOH} + wt_{n-p}} \times 100\%,$$

where j_i is partial current density of specific liquid product, u is the electrolyte flow rate, n_i is the number of electrons involved, and M is the molar mass.

One-dimensional ^{1}H NMR spectra were collected on a Bruker AVIII 500-MHz NMR spectrometer with solvent (water) suppression to quantify the liquid products. Typically, 500 μL of electrolyte collected at each potential was mixed with 100 μL of D_2O and 0.05 μL dimethyl sulfoxide (DMSO) as internal standard. Standard curves were made accordingly by mixing DMSO with known concentrations of certain chemicals at the range of interest.

Density Functional Theory. Density functional theory, implemented in the Vienna ab initio Simulation Package (VASP 5.4.4) (80), was used to calculate the energy of the systems with adsorbates on the copper surfaces. The core electrons were treated with the projector augmented-wave (PAW) (81) method and default potentials in VASP (82). The explicit valence electrons of each element were as follows: C, $2s^22p^2$; Cu, $4s^13d^{10}$; H, $1s^1$; and O, $2s^22p^4$. The generalized gradient approximation (GGA) method with the Perdew–Burke–Ernzerhof (PBE) (83) exchange-correlation functional was applied with spin polarization. Monkhorst–Pack (MP) (84) k-point samplings were 5 × 5 × 1 for Cu(100), 8 × 4 × 1 for Cu(611) and pocket-shape surfaces, and 8 × 8 × 1 for Cu(211). Planewave basis sets were truncated at 400 eV. The dipole correction was applied along the z direction normal to the slab model. Grimme D3 dispersion was used to treat van der Waals interactions (85). Once the geometries were optimized in vacuum, solvation was treated implicitly using VASPsol (86, 87) with a dielectric constant of 78.4 for water as a single-point correction. All of the geometries were optimized until the maximum force between the atoms was 0.01 eV·$Å^{-1}$ (0.05 eV·$Å^{-1}$ for transition states) and were confirmed via frequency analysis. The energy of hydrogen was calculated using a 15 × 16 × 17 $Å^3$ simulation cell with 1 × 1 × 1 MP sampling. To calculate the Gibbs free energy, corrections were computed using the standard formulas derived from statistical mechanics. Translation, rotational, and vibrational contributions were included for gas-phase H_2, while only vibrational contributions were considered for adsorbed species. All of the calculated free energies with solvation correction, the imaginary frequencies of the transition state, and the relevant geometries are reported in *SI Appendix*, Table S5 and the online repository (https://github.com/tsenftle/CO_Acetate).

The copper surfaces were represented by three layers of Cu(100) as shown in *SI Appendix*, Fig. S22*A*, where the bottom layer was fixed. The Cu(611) facet represented the step surface separating (111) and (100) surface facets (*SI Appendix*, Fig. S22*B*), which has been used in previous literature to as a step model to study the dissociation of CO_2 on Cu(100) surfaces (73). The pocket-shape surface was modified from Cu(611) by adding one more Cu layer on the step defect (*SI Appendix*, Fig. S22*C*), while Cu(211) represented the step surface that adsorbs species on (111) and has (100) as the step (*SI Appendix*, Fig. S22*D*). The transition states were found using the climbing image nudge elastic band (CI-NEB) method (88). For computing electrochemical barriers, we applied the method developed by Janik and coworkers (89–92). Specific details of the electrochemical barrier calculations are reported in *SI Appendix*.

Data Availability. All study data are included in this article and *SI Appendix* and in https://github.com/tsenftle/CO_Acetate.

ACKNOWLEDGMENTS. This work was supported by NSF Grant 2029442 and Rice University. H.W. is a Canadian Institute for Advanced Research (CIFAR) Azrieli Global Scholar in the Bio-Inspired Solar Energy Program. C.X. acknowledges support from a J. Evans Attwell-Welch postdoctoral fellowship provided by the Smalley-Curl Institute. This work was performed in part at the Shared Equipment Authority at Rice University. The authors acknowledge the use of Electron Microscopy Center (EMC) at Rice University. Y.L. and H.N.A. acknowledge the support from King Abdullah University of Science and Technology. T.P.S. and C.-Y.L. acknowledge startup funding from Rice University.

1. B. Obama, The irreversible momentum of clean energy. *Science* **355**, 126–129 (2017).
2. H. R. Jhong, S. C. Ma, P. J. A. Kenis, Electrochemical conversion of CO_2 to useful chemicals: Current status, remaining challenges, and future opportunities. *Curr. Opin. Chem. Eng.* **2**, 191–199 (2013).
3. A. M. Appel *et al.*, Frontiers, opportunities, and challenges in biochemical and chemical catalysis of CO_2 fixation. *Chem. Rev.* **113**, 6621–6658 (2013).
4. S. Chu, Y. Cui, N. Liu, The path towards sustainable energy. *Nat. Mater.* **16**, 16–22 (2016).
5. S. Verma, S. Lu, P. J. A. Kenis, Co-electrolysis of CO_2 and glycerol as a pathway to carbon chemicals with improved technoeconomics due to low electricity consumption. *Nat. Energy* **4**, 466–474 (2019).
6. J. Gu, C.-S. Hsu, L. Bai, H. M. Chen, X. Hu, Atomically dispersed Fe^{3+} sites catalyze efficient CO_2 electroreduction to CO. *Science* **364**, 1091–1094 (2019).

7. Y. Pang *et al*., Efficient electrocatalytic conversion of carbon monoxide to propanol using fragmented copper. *Nat. Catal.* **2**, 251–258 (2019).
8. M. B. Ross *et al*., Designing materials for electrochemical carbon dioxide recycling. *Nat. Catal.* **2**, 648–658 (2019).
9. D. Gao, R. M. Arán-Ais, H. S. Jeon, B. Roldan Cuenya, Rational catalyst and electrolyte design for CO_2 electroreduction towards multicarbon products. *Nat. Catal.* **2**, 198–210 (2019).
10. Y. Chen, C. W. Li, M. W. Kanan, Aqueous CO_2 reduction at very low overpotential on oxide-derived Au nanoparticles. *J. Am. Chem. Soc.* **134**, 19969–19972 (2012).
11. N. Han *et al*., Ultrathin bismuth nanosheets from in situ topotactic transformation for selective electrocatalytic CO_2 reduction to formate. *Nat. Commun.* **9**, 1320 (2018).
12. Y. Wu, Z. Jiang, X. Lu, Y. Liang, H. Wang, Domino electroreduction of CO_2 to methanol on a molecular catalyst. *Nature* **575**, 639–642 (2019).
13. S. Gao *et al*., Partially oxidized atomic cobalt layers for carbon dioxide electroreduction to liquid fuel. *Nature* **529**, 68–71 (2016).
14. C. Zhao *et al*., Ionic exchange of metal-organic frameworks to access single nickel sites for efficient electroreduction of CO_2. *J. Am. Chem. Soc.* **139**, 8078–8081 (2017).
15. C. W. Li, M. W. Kanan, CO_2 reduction at low overpotential on Cu electrodes resulting from the reduction of thick Cu_2O films. *J. Am. Chem. Soc.* **134**, 7231–7234 (2012).
16. D. Kim, C. S. Kley, Y. Li, P. Yang, Copper nanoparticle ensembles for selective electroreduction of CO_2 to C_2-C_3 products. *Proc. Natl. Acad. Sci. U.S.A.* **114**, 10560–10565 (2017).
17. M. Ma, K. Djanashvili, W. A. Smith, Controllable hydrocarbon formation from the electrochemical reduction of CO_2 over Cu nanowire arrays. *Angew. Chem. Int. Ed. Engl.* **55**, 6680–6684 (2016).
18. M. Jouny, W. Luc, F. Jiao, High-rate electroreduction of carbon monoxide to multicarbon products. *Nat. Catal.* **1**, 748–755 (2018).
19. A. Dutta, M. Rahaman, N. C. Luedi, P. Broekmann, Morphology matters: Tuning the product distribution of CO_2 electroreduction on oxide-derived Cu foam catalysts. *ACS Catal.* **6**, 3804–3814 (2016).
20. Y. Lum, B. Yue, P. Lobaccaro, A. T. Bell, J. W. Ager, Optimizing C–C coupling on oxide-derived copper catalysts for electrochemical CO_2 reduction. *J. Phys. Chem. C* **121**, 14191–14203 (2017).
21. R. Kortlever, J. Shen, K. J. P. Schouten, F. Calle-Vallejo, M. T. M. Koper, Catalysts and reaction pathways for the electrochemical reduction of carbon dioxide. *J. Phys. Chem. Lett.* **6**, 4073–4082 (2015).
22. K. J. P. Schouten, Y. Kwon, C. J. M. van der Ham, Z. Qin, M. T. M. Koper, A new mechanism for the selectivity to C_1 and C_2 species in the electrochemical reduction of carbon dioxide on copper electrodes. *Chem. Sci. (Camb.)* **2**, 1902–1909 (2011).
23. Y. Jiao, Y. Zheng, P. Chen, M. Jaroniec, S.-Z. Qiao, Molecular scaffolding strategy with synergistic active centers to facilitate electrocatalytic CO_2 reduction to hydrocarbon/alcohol. *J. Am. Chem. Soc.* **139**, 18093–18100 (2017).
24. M. Jouny, G. S. Hutchings, F. Jiao, Carbon monoxide electroreduction as an emerging platform for carbon utilization. *Nat. Catal.* **2**, 1062–1070 (2019).
25. H. Zhang, J. Li, M.-J. Cheng, Q. C. O. Lu, Electroreduction: Current development and understanding of Cu-based catalysts. *ACS Catal.* **9**, 49–65 (2018).
26. K. Jiang *et al*., Metal ion cycling of Cu foil for selective C-C coupling in electrochemical CO2 reduction. *Nat. Catal.* **1**, 111–119 (2018).
27. A. Loiudice *et al*., Tailoring copper nanocrystals towards C_2 products in electrochemical CO_2 reduction. *Angew. Chem. Int. Ed. Engl.* **55**, 5789–5792 (2016).
28. Z. Wang, G. Yang, Z. Zhang, M. Jin, Y. Yin, Selectivity on etching: Creation of high-energy facets on copper nanocrystals for CO_2 electrochemical reduction. *ACS Nano* **10**, 4559–4564 (2016).
29. C. W. Li, J. Ciston, M. W. Kanan, Electroreduction of carbon monoxide to liquid fuel on oxide-derived nanocrystalline copper. *Nature* **508**, 504–507 (2014).
30. D. Ren *et al*., Selective electrochemical reduction of carbon dioxide to ethylene and ethanol on copper(I) oxide catalysts. *ACS Catal.* **5**, 2814–2821 (2015).
31. S. Lee, D. Kim, J. Lee, Electrocatalytic production of C_3-C_4 compounds by conversion of CO_2 on a chloride-induced Bi-phasic Cu_2O-Cu catalyst. *Angew. Chem. Int. Ed. Engl.* **54**, 14701–14705 (2015).
32. H. Mistry *et al*., Highly selective plasma-activated copper catalysts for carbon dioxide reduction to ethylene. *Nat. Commun.* **7**, 12123 (2016).
33. Z. Weng *et al*., Self-cleaning catalyst electrodes for stabilized CO_2 reduction to hydrocarbons. *Angew. Chem. Int. Ed. Engl.* **56**, 13135–13139 (2017).
34. F. Calle-Vallejo, M. T. M. Koper, Theoretical considerations on the electroreduction of CO to C_2 species on Cu(100) electrodes. *Angew. Chem. Int. Ed. Engl.* **52**, 7282–7285 (2013).
35. M. Jouny, W. Luc, F. Jiao, General techno-economic analysis of CO_2 electrolysis systems. *Ind. Eng. Chem. Res.* **57**, 2165–2177 (2018).
36. O. S. Bushuyev *et al*., What should we make with CO_2 and how can we make it? *Joule* **2**, 825–832 (2018).
37. M. J. Orella, S. M. Brown, M. E. Leonard, Y. Román-Leshkov, F. R. Brushett, A general techno-economic model for evaluating emerging electrolytic processes. *Energy Technol. (Weinheim)* **8**, 1900994 (2019).
38. C.-T. Dinh *et al*., CO_2 electroreduction to ethylene via hydroxide-mediated copper catalysis at an abrupt interface. *Science* **360**, 783–787 (2018).
39. D. Ren, B. S.-H. Ang, B. S. Yeo, Tuning the selectivity of carbon dioxide electroreduction toward ethanol on oxide-derived Cu_xZn catalysts. *ACS Catal.* **6**, 8239–8247 (2016).
40. Y. Wang *et al*., CO_2 reduction to acetate in mixtures of ultrasmall $(Cu)_n$, $(Ag)_m$ bimetallic nanoparticles. *Proc. Natl. Acad. Sci. U.S.A.* **115**, 278–283 (2018).
41. W. Luc *et al*., Two-dimensional copper nanosheets for electrochemical reduction of carbon monoxide to acetate. *Nat. Catal.* **2**, 423–430 (2019).
42. Y. Wang *et al*., Copper nanocubes for CO_2 reduction in gas diffusion electrodes. *Nano Lett.* **19**, 8461–8468 (2019).
43. A. S. Malkani, M. Dunwell, B. Xu, Operando spectroscopic investigations of copper and oxide-derived copper catalysts for electrochemical CO reduction. *ACS Catal.* **9**, 474–478 (2019).
44. C. Choi *et al*., Highly active and stable stepped Cu surface for enhanced electrochemical CO_2 reduction to C_2H_4. *Nat. Catal.* **3**, 804–812 (2020).
45. T. M. Gür, Review of electrical energy storage technologies, materials and systems: Challenges and prospects for large-scale grid storage. *Energy Environ. Sci.* **11**, 2696–2767 (2018).
46. Y. C. Li *et al*., Binding site diversity promotes CO_2 electroreduction to ethanol. *J. Am. Chem. Soc.* **141**, 8584–8591 (2019).
47. E. L. Clark, C. Hahn, T. F. Jaramillo, A. T. Bell, Electrochemical CO_2 reduction over compressively strained CuAg surface alloys with enhanced multi-carbon oxygenate selectivity. *J. Am. Chem. Soc.* **139**, 15848–15857 (2017).
48. C. Xia *et al*., Continuous production of pure liquid fuel solutions via electrocatalytic CO_2 reduction using solid-electrolyte devices. *Nat. Energy* **4**, 776–785 (2019).
49. C. Xia, Y. Xia, P. Zhu, L. Fan, H. Wang, Direct electrosynthesis of pure aqueous H_2O_2 solutions up to 20% by weight using a solid electrolyte. *Science* **366**, 226–231 (2019).
50. Y. Sui *et al*., Low temperature synthesis of Cu_2O crystals: Shape evolution and growth mechanism. *Cryst. Growth Des.* **10**, 99–108 (2010).
51. I. C. Chang *et al*., Large-scale synthesis of uniform Cu_2O nanocubes with tunable sizes by in-situ nucleation. *CrystEngComm* **15**, 2363–2366 (2013).
52. D.-Y. Wu, J.-F. Li, B. Ren, Z.-Q. Tian, Electrochemical surface-enhanced Raman spectroscopy of nanostructures. *Chem. Soc. Rev.* **37**, 1025–1041 (2008).
53. A. Dutta, A. Kuzume, M. Rahaman, S. Vesztergom, P. Broekmann, Monitoring the chemical state of catalysts for CO_2 electroreduction: An in operando study. *ACS Catal.* **5**, 7498–7502 (2015).
54. Y. L. Deng, A. D. Handoko, Y. H. Du, S. B. Xi, B. S. Yeo, In situ Raman spectroscopy of copper and copper oxide surfaces during electrochemical oxygen evolution reaction: Identification of Cu-III oxides as catalytically active species. *ACS Catal.* **6**, 2473–2481 (2016).
55. A. Eilert *et al*., Subsurface oxygen in oxide-derived copper electrocatalysts for carbon dioxide reduction. *J. Phys. Chem. Lett.* **8**, 285–290 (2017).
56. Y. Lum, J. W. Ager, Stability of residual oxides in oxide-derived copper catalysts for electrochemical CO_2 reduction investigated with ^{18}O labeling. *Angew. Chem. Int. Ed. Engl.* **57**, 551–554 (2018).
57. Y. Zhao *et al*., Speciation of Cu surfaces during the electrochemical CO reduction reaction. *J. Am. Chem. Soc.* **142**, 9735–9743 (2020).
58. N. Ikemiya, T. Kubo, S. Hara, In situ AFM observations of oxide film formation on Cu (111) and Cu (100) surfaces under aqueous alkaline solutions. *Surf. Sci.* **323**, 81–90 (1995).
59. G. Zhou, J. C. Yang, Formation of quasi-one-dimensional Cu_2O structures by in situ oxidation of Cu(100). *Phys. Rev. Lett.* **89**, 106101 (2002).
60. R. Reske, H. Mistry, F. Behafarid, B. Roldan Cuenya, P. Strasser, Particle size effects in the catalytic electroreduction of CO_2 on Cu nanoparticles. *J. Am. Chem. Soc.* **136**, 6978–6986 (2014).
61. Y. Hori, H. Wakebe, T. Tsukamoto, O. Koga, Electrocatalytic process of CO selectivity in electrochemical reduction of CO_2 at metal electrodes in aqueous media. *Electrochim. Acta* **39**, 1833–1839 (1994).
62. Y. Hori, K. Kikuchi, S. Suzuki, Production of CO and CH_4 in electrochemical reduction of CO_2 at metal electrodes in aqueous hydrogencarbonate solution. *Chem. Lett.* **14**, 1695–1698 (1985).
63. Y. Lee, J. Suntivich, K. J. May, E. E. Perry, Y. Shao-Horn, Synthesis and activities of rutile IrO2 and RuO2 nanoparticles for oxygen evolution in acid and alkaline solutions. *J. Phys. Chem. Lett.* **3**, 399–404 (2012).
64. E. Bertheussen *et al*., Acetaldehyde as an intermediate in the electroreduction of carbon monoxide to ethanol on oxide-derived copper. *Angew. Chem. Int. Ed. Engl.* **55**, 1450–1454 (2016).
65. E. Pérez-Gallent, M. C. Figueiredo, F. Calle-Vallejo, M. T. M. Koper, Spectroscopic observation of a hydrogenated CO dimer intermediate during CO reduction on Cu(100) electrodes. *Angew. Chem. Int. Ed. Engl.* **56**, 3621–3624 (2017).
66. H. Xiao, T. Cheng, W. A. Goddard, Atomistic mechanisms underlying selectivities in $C(_1)$ and $C(_2)$ products from electrochemical reduction of CO on Cu(111). *J. Am. Chem. Soc.* **139**, 130–136 (2017).
67. T. Cheng, H. Xiao, W. A. Goddard, Full atomistic reaction mechanism with kinetics for CO reduction on Cu(100) from ab initio molecular dynamics free-energy calculations at 298 K. *Proc. Natl. Acad. Sci. U.S.A.* **114**, 1795–1800 (2017).
68. Y. Lum, T. Cheng, W. A. Goddard, J. W. Ager, Electrochemical CO reduction builds solvent water into oxygenate products. *J. Am. Chem. Soc.* **140**, 9337–9340 (2018).
69. W. Luo, X. Nie, M. J. Janik, A. Asthagiri, Facet dependence of CO_2 reduction paths on Cu electrodes. *ACS Catal.* **6**, 219–229 (2016).
70. A. Bagger, W. Ju, A. S. Varela, P. Strasser, J. Rossmeisl, Electrochemical CO_2 reduction: Classifying Cu facets. *ACS Catal.* **9**, 7894–7899 (2019).
71. Y. Huang, Y. Chen, T. Cheng, L.-W. Wang, W. A. Goddard, Identification of the selective sites for electrochemical reduction of CO to C_{2+} products on copper nanoparticles by combining reactive force fields, density functional theory, and machine learning. *ACS Energy Lett.* **3**, 2983–2988 (2018).
72. K. Jiang *et al*., Effects of surface roughness on the electrochemical reduction of CO_2 over Cu. *ACS Energy Lett.* **5**, 1206–1214 (2020).
73. B. Hagman *et al*., Steps control the dissociation of CO_2 on Cu(100). *J. Am. Chem. Soc.* **140**, 12974–12979 (2018).
74. Y. Y. Birdja *et al*., Advances and challenges in understanding the electrocatalytic conversion of carbon dioxide to fuels. *Nat. Energy* **4**, 732–745 (2019).
75. J. Zhao *et al*., An overview of Cu-based heterogeneous electrocatalysts for CO_2 reduction. *J. Mater. Chem. A* **8**, 4700–4734 (2020).

76. A. J. Garza, A. T. Bell, M. Head-Gordon, Mechanism of CO_2 reduction at copper surfaces: Pathways to C_2 products. *ACS Catal.* **8**, 1490–1499 (2018).
77. P. Grosse *et al*., Dynamic changes in the structure, chemical state and catalytic selectivity of Cu nanocubes during CO_2 electroreduction: Size and support effects. *Angew. Chem. Int. Ed. Engl.* **57**, 6192–6197 (2018).
78. J. J. Kaczur, H. Yang, Z. Liu, S. D. Sajjad, R. I. Masel, Carbon dioxide and water electrolysis using new alkaline stable anion membranes. *Front Chem.* **6**, 263 (2018).
79. Z. Liu, H. Yang, R. Kutz, R. I. Masel, CO_2 electrolysis to CO and O_2 at high selectivity, stability and efficiency using sustainion membranes. *J. Electrochem. Soc.* **165**, J3371–J3377 (2018).
80. G. Kresse, J. Furthmüller, Efficient iterative schemes for ab initio total-energy calculations using a plane-wave basis set. *Phys. Rev. B Condens. Matter* **54**, 11169–11186 (1996).
81. P. E. Blöchl, Projector augmented-wave method. *Phys. Rev. B Condens. Matter* **50**, 17953–17979 (1994).
82. G. Kresse, D. Joubert, From ultrasoft pseudopotentials to the projector augmented-wave method. *Phys. Rev. B* **59**, 1758–1775 (1999).
83. J. P. Perdew, K. Burke, M. Ernzerhof, Generalized gradient approximation made simple. *Phys. Rev. Lett.* **77**, 3865–3868 (1996).
84. H. J. Monkhorst, J. D. Pack, Special points for Brillouin-zone integrations. *Phys. Rev. B* **13**, 5188–5192 (1976).
85. S. Grimme, J. Antony, S. Ehrlich, H. Krieg, A consistent and accurate ab initio parametrization of density functional dispersion correction (DFT-D) for the 94 elements H-Pu. *J. Chem. Phys.* **132**, 154104 (2010).
86. K. Mathew, R. Sundararaman, K. Letchworth-Weaver, T. A. Arias, R. G. Hennig, Implicit solvation model for density-functional study of nanocrystal surfaces and reaction pathways. *J. Chem. Phys.* **140**, 084106 (2014).
87. K. Mathew, V. S. C. Kolluru, S. Mula, S. N. Steinmann, R. G. Hennig, Implicit self-consistent electrolyte model in plane-wave density-functional theory. *J. Chem. Phys.* **151**, 234101 (2019).
88. G. Henkelman, B. P. Uberuaga, H. Jónsson, A climbing image nudged elastic band method for finding saddle points and minimum energy paths. *J. Chem. Phys.* **113**, 9901–9904 (2000).
89. G. Rostamikia, A. J. Mendoza, M. A. Hickner, M. J. Janik, First-principles based microkinetic modeling of borohydride oxidation on a Au(111) electrode. *J. Power Sources* **196**, 9228–9237 (2011).
90. X. Nie, M. R. Esopi, M. J. Janik, A. Asthagiri, Selectivity of $CO(_2)$ reduction on copper electrodes: The role of the kinetics of elementary steps. *Angew. Chem. Int. Ed. Engl.* **52**, 2459–2462 (2013).
91. S. A. Akhade, N. J. Bernstein, M. R. Esopi, M. J. Regula, M. J. Janik, A simple method to approximate electrode potential-dependent activation energies using density functional theory. *Catal. Today* **288**, 63–73 (2017).
92. S. Maheshwari, Y. Li, N. Agrawal, M. J. Janik, "Density functional theory models for electrocatalytic reactions" in *Advances in Catalysis*, C. Song, Ed. (Academic Press, 2018), vol. 63, pp. 117–167.